



Metal-defected spinel $Mn_xCo_{3-x}O_4$ with octahedral Mn-enriched surface for highly efficient oxygen reduction reaction

Ke Li^{a,b,1}, Rongrong Zhang^{a,b,1}, Ruijie Gao^{a,b}, Guo-Qiang Shen^{a,b}, Lun Pan^{a,b,*}, Yunduo Yao^{a,b}, Kaihui Yu^a, Xiangwen Zhang^{a,b}, Ji-Jun Zou^{a,b,*}

^a Key Laboratory for Green Chemical Technology of the Ministry of Education, School of Chemical Engineering and Technology, Tianjin University, Tianjin, 300072, China

^b Collaborative Innovative Center of Chemical Science and Engineering (Tianjin), Tianjin, 300072, China



ARTICLE INFO

Keywords:

Manganese-cobalt oxide
Spinel
Metal defect engineering
ORR

ABSTRACT

Manganese-cobalt spinel oxides are considered as a class of promising and low-cost electrocatalysts for oxygen reduction reaction (ORR), whose performances largely depend on their electronic structures which can be effectively optimized by defect engineering. Herein, metal defects (manganese vacancies and cobalt vacancies, *i.e.* V_{Mn} and V_{Co}) were *in-situ* introduced into spinel $Mn_xCo_{3-x}O_4$ via a simple solvothermal treatment followed by thermal calcination. Mn-Co glycerolate precursors not only enable controllable synthesis of spinel oxides with variable metallic ratios, but also play a key role in constructing metal defected crystals for their lamellated structure. As a result of the formation rate difference between manganese and cobalt glycerolate, a unique Mn-enriched surface is formed, leading to the increase of highly active sites for ORR. Importantly, the presence of metal defects, confirmed by XRD (X-ray diffraction), element analysis and XAFS (X-ray absorption fine structure spectroscopy), leads to greatly increased electrical conductivity and O_2 adsorption ability, thus bringing about enhanced ORR activity. Especially, metal-defected $Mn_{1.5}Co_{1.5}O_4$, with the optimal Mn/Co ratio, exhibits comparable activity and superior durability to those of the benchmark Pt/C in ORR and displays excellent discharge performance in Zn-air batteries for practical application. This work provides a new way to optimize the electrocatalytic performance of mixed metal spinel oxides *via* rational defect engineering.

1. Introduction

Driven by imminent shortage of fossil fuels and growing environmental concerns, extensive efforts have been made to develop a new generation of sustainable, clean and highly efficient energy conversion and storage technologies, such as fuel cells and metal-air batteries [1–4]. However, due to a complex multistep four-electron process, kinetically sluggish oxygen reduction reaction (ORR) at the cathode is a bottleneck limiting the efficiency of such electrochemical energy devices. And it often requires high overpotentials, which can be ameliorated with the assistance of efficient electrocatalysts [5–7]. Currently, noble-metal-based catalysts such as platinum (Pt) and its alloys are regarded as the benchmark catalysts for ORR, but their high cost, scarce reserves and poor stability severely hinder their large-scale application [8]. With considerable activity and superior durability, the low-cost earth-abundant transition metal oxides, such as the most investigated Mn- and Co-based oxides with spinel [9–14], perovskite [1,2,15] and

rock-salt structure [16–18], are considered as promising alternatives.

Spinel oxides consisting of metal cations occupying tetrahedral (four-coordination) and octahedral (six-coordination) sites are increasingly attractive owing to their multi-valence, controllable compositions and structures [19], among which Mn_3O_4 [20,21] and Co_3O_4 [11,22] have been extensively investigated. However, their performances are still far below expectations because of intrinsically large band gap that in turn causes low electrical conductivity and poor O_2^- -binding/activating ability [5]. Introducing a second metal ion to form mixed spinel oxides is an effective way to improve ORR activity as a result of enriched electroactive sites for adsorption/activation of oxygen and improved electrical conductivity through electron hopping among multi-valence cations [23,24]. Combining two of the most electroactive metal species, manganese-cobalt spinel oxide ($Mn_xCo_{3-x}O_4$) is considered as one of the most promising catalysts towards ORR and its performance largely depends on the composition and electronic structure which are strongly correlated with electrical conductivity and

* Corresponding authors at: Key Laboratory for Green Chemical Technology of the Ministry of Education, School of Chemical Engineering and Technology, Tianjin University, Tianjin, 300072, China.

E-mail addresses: panlun76@tju.edu.cn (L. Pan), jj_zou@tju.edu.cn (J.-J. Zou).

¹ These authors contributed equally to this work.

oxygen adsorption capability [25].

Meanwhile, engineering metal defects is an effective way to regulate the electronic structure and optimize active sites even with trace concentrations [26,27]. For one thing, metal defects can lead to half-metalllicity [26] and obvious electronic delocalization [28], which are closely associated with a decreased bandgap and increased density of electronic states around the Fermi level, thus improving the electrical conductivity. For another thing, O₂ adsorption and activation will be optimized with the presence of metal defects, owing to the increased number of active sites as well as the optimization of reaction energy barrier [25] and σ^* -orbital (e_g) occupancy of active cations [1,29,30]. Thus, since electrical conductivity and oxygen adsorption ability are two key points that influence the performance of ORR catalysts [19], the construction of defected crystals is an ideal way to promote ORR activity. Actually, in our previous work, we have developed a universal and stable way to fabricate metal defects in single metal oxides such as ZnO [31], TiO₂ [32] and Co₃O₄ [28], which all show significantly enhanced activity in photocatalysis and electrocatalysis. Through the thermal calcination of metal glycerolates, various metal defects are *in-situ* constructed by the bonding between terminal retained O atoms of glycerin groups and M–O–M (M: metal) skeleton lamellas. In this process, the resulting O-rich structure stimulates the formation of metal voids.

Accordingly, in this work, we extend this method to mixed metal oxide and successfully *in-situ* introduce metal vacancies of V_{Mn} and V_{Co} into bimetallic spinel Mn_xCo_{3-x}O₄ via a simple solvothermal approach followed by thermal calcination. The key point is the use of bimetal glycerolates as precursors to achieve controllable metallic ratios and *in-situ* introduce metal defects into the resulting spinel oxides. Meanwhile, determined by the formation rate difference of manganese and cobalt glycerolate, a unique Mn-enriched surface is formed, leading to increased surface catalytic sites and optimal bulk conductivity for ORR. More importantly, the presence of metal defects (V_{Mn} and V_{Co}) results in improved ORR activity due to greatly enhanced electrical conductivity and O₂ adsorption ability. Metal-defected Mn_{1.5}Co_{1.5}O₄, with the optimal Mn/Co ratio, exhibits a half-wave potential of 0.822 V (vs. RHE) and high limiting current density of 5.98 mA cm⁻² in ORR, outperforming the benchmark Pt/C (0.813 V and 5.68 mA cm⁻²). Furthermore, metal-defected Mn_{1.5}Co_{1.5}O₄ is catalytically efficient in Zn-air battery, offering a promising strategy for advanced cathode materials.

2. Experimental section

2.1. Materials

Manganese (II) acetate tetrahydrate (Mn(CH₃COO)₂·4H₂O), glycerol, isopropanol and ethanol were all obtained from Tianjin Guangfu Fine Chemical Research Institute. Cobalt (II) acetate tetrahydrate (Co (CH₃COO)₂·4H₂O) was purchased from Alfa Aesar. Potassium hydroxide was provided by Aladdin Industrial Corporation. 20 wt% Pt/C was supplied by Johnson Matthey. Nafion solution (5 wt%) was purchased from DuPont. Vulcan XC-72R was obtained from Carbot. Milli-Q ultrapure water (> 18.25 MΩ cm) was used in all experiments. All the chemicals were reagent grade and used as received without further purification.

2.2. Catalyst preparation

The Mn_xCo_{3-x}O₄ (x = 0, 0.6, 1.2, 1.5, 1.8, 2.4, 3) catalysts were prepared by the calcination of corresponding metal glycerolates (denoted as Mn_xCo_{3-x}Gly), where x and 3-x stand for the feeding amount of Mn and Co sources, respectively. In a typical synthesis of Mn_{1.5}Co_{1.5}O₄, 0.5 g manganese (II) acetate tetrahydrate, 0.5 g cobalt (II) acetate tetrahydrate and 30 mL glycerol were mixed in a 100 mL Teflon-lined stainless-steel autoclave under stirring for half an hour. Then the

autoclave was heated at 180 °C for 1.5 h in an oven. After that, the obtained metal glycerolates (*i.e.* Mn_{1.5}Co_{1.5}Gly) were collected, washed with ethanol, dried overnight at 60 °C, and finally calcined in air at 300 °C for 2 h (with a heating rate of 5 °C min⁻¹). Similarly, other samples (Mn_{0.6}Co_{2.4}O₄, Mn_{1.2}Co_{1.8}O₄, Mn_{1.8}Co_{1.2}O₄ and Mn_{2.4}Co_{0.6}O₄) were synthesized by adjusting the feeding ratios of manganese to cobalt sources. The total amount of metal sources was kept constant as 1 g. Pure Mn₃O₄ and Co₃O₄ were prepared by the same method, using only 1 g manganese acetate and cobalt acetate, respectively.

Moreover, Mn_{1.5}Co_{1.5}Gly was calcined at different temperatures (300 °C, 500 °C and 700 °C) for 2 h with a heating rate of 5 °C min⁻¹ in air to obtain MC-300, MC-500 and MC-700 respectively.

2.3. Characterizations

The X-ray absorption fine structure spectroscopy (XAFS) measurement was conducted on the 1W2B beamline of Beijing Synchrotron Radiation Facility, using an incident beam monochromatized by Si (111) double crystal monochromators. The storage ring runs 2.5 GeV electrons at 250 mA constantly during the measurements. Inductively coupled plasma optical emission spectrometer (ICP-OES) measurements were carried out on a VISTA-MPX EL02115765 instrument to analyze element compositions. X-ray photoelectron spectroscopy (XPS) analysis was conducted on a PHI-1600 instrument equipped with Al K α radiation and the binding energy was calibrated by the C 1 s peak (284.8 eV). X-ray diffraction (XRD) patterns were obtained by using a Bruker AXS D8 focus (D8-S4) X-ray diffractometer equipped with a nickel-filtered Cu K α radiation at a scan rate of 5° min⁻¹. Transmission electron microscopy (TEM) and corresponding energy dispersive spectrum (EDS) characterization were performed with a JEM-2100F transmission electron microscope at 200 kV. O₂ temperature programmed desorption (O₂-TPD) measurements were performed on an AutoChem II 2920 chemisorption analyzer (Micromeritics, USA). After pretreated at 200 °C in He gas for 1 h, the samples (100 mg) were cooled down. Then flowing O₂ (ultrahigh purity) through the samples for 1 h to well adsorb. Subsequently the samples were purged with He gas for 30 min to evacuate the remaining O₂. Finally, the desorption was carried out by heating up to 700 °C in He gas at a rate of 10 °C min⁻¹.

2.4. Electrochemical measurements

All the electrochemical measurements were carried out with an IVIUMSTAT workstation (Ivium Technologies BV, Netherlands) equipped with a modulated speed rotator (MSR) (Pine Research Instrumentation, Inc.) in a standard three-electrode system with 0.1 M KOH as the electrolyte, a modified glassy carbon electrode (5 mm in diameter) as the working electrode, a graphite rod as the counter electrode, and a Ag/AgCl (saturated KCl) electrode as the reference electrode. The working electrode modified with a thin catalyst film was prepared as follows. 5 mg of catalyst and 1 mg of VXC-72R C as a conductive additive were dispersed in 1 mL of isopropanol-water mixture with volume ratio of 3:1 with 50 μ L of 5 wt% Nafion solution to form a homogeneous ink by ultrasonic dispersion. Then 10 μ L of the catalyst ink was dropped onto a newly polished glassy-carbon electrode and dried under room temperature. The ink of the benchmark 20 wt% Pt/C was prepared as the same procedure. Before each measurement, the electrolyte was purged with O₂ or Ar for at least 30 min. All data were reported without iR compensation.

3. Results and discussion

3.1. Crystal structure of Mn_xCo_{3-x}O₄ with Mn-enriched surface

Initially, glycerolate precursors (Mn_xCo_{3-x}Gly) were fabricated by solvothermal treatment of manganese acetate and (or) cobalt acetate in glycerol. As shown in Fig. 1a (XRD patterns), all the precursors show a

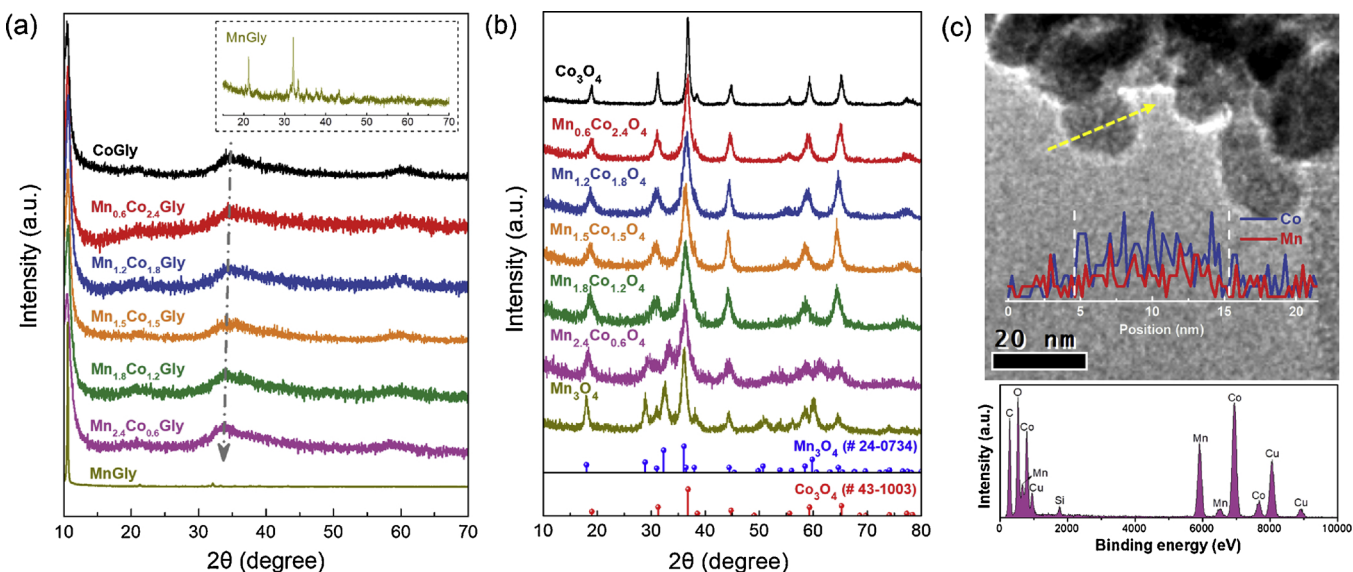


Fig. 1. XRD patterns of (a) glycerolate precursors ($Mn_xCo_{3-x}Gly$) (Inset is the magnified parts of MnGly above 15°) and (b) corresponding $Mn_xCo_{3-x}O_4$ ($x = 0-3$) with different molar ratios of Mn to Co. (c) TEM image and corresponding EDS and line scan analysis of $Mn_{1.5}Co_{1.5}O_4$.

sharp peak at *ca.* 10° , which is the characteristic of layered structure of metal glycerolates [33] and benefits the formation of metal defects during thermal calcination [28]. The diffraction pattern of CoGly has three broad peaks at about 21° , 35° and 60.7° , consistent with reported results [28,33]. For MnGly, there are several intense peaks in the range of $20-40^\circ$ (inset of Fig. 1a), corresponding to manganese (II) glycerolate [33,34]. Moreover, the diffraction patterns of bimetal glycerolates are very similar to that of CoGly, but gradually shift to smaller angles with the increase of Mn content, which can be ascribed to the enlarged cell parameters caused by substitution of Co sites by Mn cations with larger size [10,13]. These results indicate that Mn cations diffuse into the CoGly-like lattice and substitute for Co sites during the formation of bimetal glycerolate precursors.

After thermal calcination of glycerolates at $300^\circ C$, a series of $Mn_xCo_{3-x}O_4$ with different Mn/Co ratios were obtained. As shown in Fig. 1b, all bimetal oxides possess a well-retained spinel structure and undergo a cubic-tetragonal phase transformation depending on the composition of Mn/Co. When Mn content is low ($x < 1.8$), the diffraction patterns show a typical cubic phase without any other phases and impurities, corresponding to the space group Fd-3m (no.227) [13]. It is obvious that the peak positions of these cubic spinels shift to smaller angles as the Mn content increases, confirming the incorporation of larger sized Mn cations into cubic Co_3O_4 lattice. When the Mn content is high ($x \geq 2.4$), the tetragonal phase is obtained, which can be indexed to space group I41/amd (no.141). Previous studies have shown that a cubic phase with a stronger O_2 binding ability favors ORR activity [13].

The detailed surface and bulk compositions of $Mn_xCo_{3-x}O_4$ are listed in Table 1. Both ICP and EDS results show that the bulk Mn/Co molar ratios are almost half of the designed ratios, indicating that half of the Mn sources cannot incorporate into the bulk lattice. Interestingly, the surface Mn/Co ratios determined by XPS are close to the designed compositions. A typical example is $Mn_{1.5}Co_{1.5}O_4$, whose atomic ratios of Mn/Co are near 1/2 in bulk but 1/1 on the surface. Meanwhile, the identical result is obtained in TEM line scan analysis (Fig. 1c). Thus, the structure of $Mn_{1.5}Co_{1.5}O_4$ should be $MnCo_2O_4$ in bulk but $Mn_{1.5}Co_{1.5}O_4$ on the surface. Among the range of cobalt manganese spinel compositions, the highest electrical conductivity was achieved for $MnCo_2O_4$ [35], thus promoting electron transfer through the bulk. Besides, higher surface Mn concentration and valence benefit ORR activity because of the governing role of more active Mn species and stronger O_2 binding ability [13,36]. The above findings imply that Mn-Co bimetal oxides

possess different surface and bulk compositions with more Mn enriched on the surface due to the formation rate difference of MnGly and CoGly which is confirmed by more Mn produced in glycerolate precipitation and the slowing growth in yields of glycerolates as the reaction proceeds (Fig. S2-3). This unique Mn-enrichment leads to optimal bulk conductivity and abundant surface active sites, which are beneficial to ORR.

3.2. Manganese and cobalt vacancies in $Mn_xCo_{3-x}O_4$

Recently, we have fabricated metal-defected ZnO [31], TiO_2 [32] and Co_3O_4 [28] by calcining metal glycerolates, where the lamellated O-rich structure plays a crucial role in the formation of metal defects. The crystal structure of metal glycerolates [37–40] is known to consist of two-dimensional polymeric sheets consisting of transition metal ions and bridging glycerol (Fig. S4). Actually, metal defects are *in-situ* constructed by the bonding between terminal retained O atoms of glycerin groups and M–O–M (M: metal) skeleton lamellas during thermal calcination [28,31,32], and thus the resulting O-rich circumstance stimulates the formation of metal voids [32,41,42].

ICP and XPS measurements were applied to determine the bulk and surface atomic ratios of metal to oxygen, respectively. As shown in Table 1, the (Mn + Co)/O ratios of surface and bulk are all lower than that of the stoichiometric $(Mn,Co)_3O_4$ (*i.e.* 0.75), suggesting the presence of metal defects. From Fig. 2a and Table 1, the total metal defect concentrations of $Mn_xCo_{3-x}O_4$ with different Mn content (including defected Mn_3O_4 and Co_3O_4) are almost constant, implying the coexistence of manganese and cobalt vacancies with equal formation possibility. Furthermore, Mn/O and Co/O ratios were calculated to identify the content of manganese vacancies (V_{Mn}) and cobalt vacancies (V_{Co}). Compared with the stoichiometric $(Mn,Co)_3O_4$, metal-defected $Mn_xCo_{3-x}O_4$ show relatively lower Mn/O and Co/O ratios (Table S1, Supplementary Material), confirming the presence of both V_{Mn} and V_{Co} . It can be seen that the content of V_{Mn} and V_{Co} have obviously positive correlation with Mn and Co content, respectively (Fig. 2b).

Then, the extended X-ray absorption fine structure (EXAFS) spectra were recorded to finely investigate the coordination structure in $Mn_{1.5}Co_{1.5}O_4$ (Fig. 3a, b). The first peak around 1.5 \AA represents M–O (metal–oxygen) bond [28,43], while the next region between 2.5 and 4 \AA represents the M–M (metal–metal) distances [43]. For $Mn_{1.5}Co_{1.5}O_4$, the FT (Fourier Transform) of the Co EXAFS spectrum looks similar to that of Co_3O_4 (Fig. 3b), while the FT spectrum of Mn

Table 1Surface and bulk elemental compositions of $Mn_xCo_{3-x}O_4$ ($x = 0.6\text{--}2.4$) determined by ICP-OES, TEM-EDS and XPS analysis.

Samples ^a	Surface ^b	Bulk ^b	Mn/Co atomic ratio	(Mn + Co)/O atomic ratio			Defect concn. ^e (%)	
				designed ratio	XPS	ICP	EDS	XPS ^c
$Mn_{0.6}Co_{2.4}O_4$	$Mn_{0.63}Co_{2.37}O_4$	$Mn_{0.46}Co_{2.54}O_4$	0.26	0.29	0.18	0.18	0.64	0.61
$Mn_{1.2}Co_{1.8}O_4$	$Mn_{1.11}Co_{1.89}O_4$	$Mn_{0.93}Co_{2.07}O_4$	0.68	0.59	0.45	0.47	0.63	0.60
$Mn_{1.5}Co_{1.5}O_4$	$Mn_{1.51}Co_{1.49}O_4$	$Mn_{1.11}Co_{1.89}O_4$	1.03	1.02	0.59	0.56	0.63	0.61
$Mn_{1.8}Co_{1.2}O_4$	$Mn_{1.66}Co_{1.34}O_4$	$Mn_{1.41}Co_{1.59}O_4$	1.54	1.23	0.88	0.87	0.62	0.58
$Mn_{2.4}Co_{0.6}O_4$	$Mn_{2.40}Co_{0.60}O_4$	$Mn_{2.09}Co_{0.91}O_4$	4.11	3.63	2.31	2.28	0.65	0.62
Mn_3O_4	–	–	–	–	–	–	0.65	0.63
Co_3O_4	–	–	–	–	–	–	0.61	0.60

^a The samples' formulas are based on the feeding molar ratios of manganese and cobalt salts.^b Chemical formulas for surface and bulk are derived from the measured Mn/Co (XPS for surface; ICP for bulk) on the basis of stoichiometric $(Mn,Co)_3O_4$ without metal defects.^c O is the lattice oxygen derived from O 1 s XPS spectra.^d The O content which can't be directly measured by ICP is obtained through deduction of Mn and Co content from the total. Samples were fully dried before weighing to avoid the extra O absorbed on the surface.^e The ratio of defect metal atoms to all atoms (see Supplementary Material for calculation details).

edge is quite different from that of Mn_3O_4 (Fig. 3a), revealing it has a similar structure to Co_3O_4 due to the same crystal phase (cubic). In particular, compared with normal Co_3O_4 , the amplitude of Co-M ($\approx 2.5\text{ \AA}$) peak in $Mn_{1.5}Co_{1.5}O_4$ declines sharply (Fig. 3b), implying lower metal coordination number (*i.e.* the number of nearest neighbor metal atoms around the absorbing Co atom) and higher mean-square disorder which further confirm the existence of metal defects. Based on the characteristic peaks of metal atoms in octahedral sites ($\approx 2.5\text{ \AA}$) and tetrahedral sites ($\approx 3.0\text{ \AA}$) [36,43–45], we can conclude that Mn cations occupy the octahedral sites, while Co cations locate at both tetragonal and octahedral sites.

Meanwhile, as shown in Mn and Co K-edge X-ray absorption near-edge structure (XANES) studies, the Mn K-edge position of $Mn_{1.5}Co_{1.5}O_4$ shifts to higher energy than reference Mn_2O_3 (Fig. 3c), suggesting that Mn^{3+} is the dominant state in $Mn_{1.5}Co_{1.5}O_4$. The Co K-edge of $Mn_{1.5}Co_{1.5}O_4$ is lower in energy than Co_3O_4 (Fig. 3d), indicating a slightly lower Co valence state than that of pure Co_3O_4 , which can be ascribed to an increase in Co^{2+}/Co^{3+} ratio due to the substitution of Mn^{3+} for Co^{3+} sites. Thus, the bulk chemical formula of $Mn_{1.5}Co_{1.5}O_4$ can be approximated as $(Co^{2+})_{\text{tet}}(Mn^{3+}Co^{3+})_{\text{oct}}O_4$, where *tet* and *oct* represent tetragonal and octahedral sites, respectively. Recent studies showed that Mn cations in octahedral sites are identified as the activity descriptor for CoMnO spinels towards oxygen electrocatalysis owing to stronger interaction between octahedrally coordinated metal cations

and oxygen [36,43]. Meanwhile, Mn cations with higher valence states [46–49] and Co^{2+} [18,50] are considered as the active sites for catalyzing ORR. Accordingly, in this work, the main existence of Mn in octahedral sites with a high valence state between +3 and +4 caused by metal defects and a slight increase in Co^{2+}/Co^{3+} ratio may contribute to excellent ORR activity.

3.3. ORR performance of metal-defected $Mn_xCo_{3-x}O_4$

The ORR catalytic performance of as-prepared $Mn_xCo_{3-x}O_4$ with different Mn/Co ratios was first evaluated by linear sweep voltammetry (LSV) on a rotating disk electrode (RDE) in O_2 -saturated 0.1 M KOH. As shown in Fig. 4a, $Mn_{1.5}Co_{1.5}O_4$ exhibits much better activity than the physical mixture of Mn_3O_4 and Co_3O_4 with a molar ratio of 1:1 (*i.e.* $Mn_3O_4 + Co_3O_4$) and corresponding monometallic counterparts in terms of more positive half-wave potential ($E_{1/2}$) and higher diffusion-limiting current density (j_L), implying that the combination of mixed metal cations can greatly enhance the ORR activity. In addition, Mn_3O_4 shows better ORR activity than Co_3O_4 , suggesting that Mn species are more active than Co. Then, the half-wave potential is used to compare ORR activity of different samples, showing a volcano-type variation trend with the Mn content in $Mn_xCo_{3-x}O_4$ (Fig. 4b, 3mA cm^{-2} is chosen for comparison due to similar j_L near 6 mA cm^{-2}). Among the samples, the highest activity is observed for $Mn_{1.5}Co_{1.5}O_4$ (0.822 V vs. RHE), which

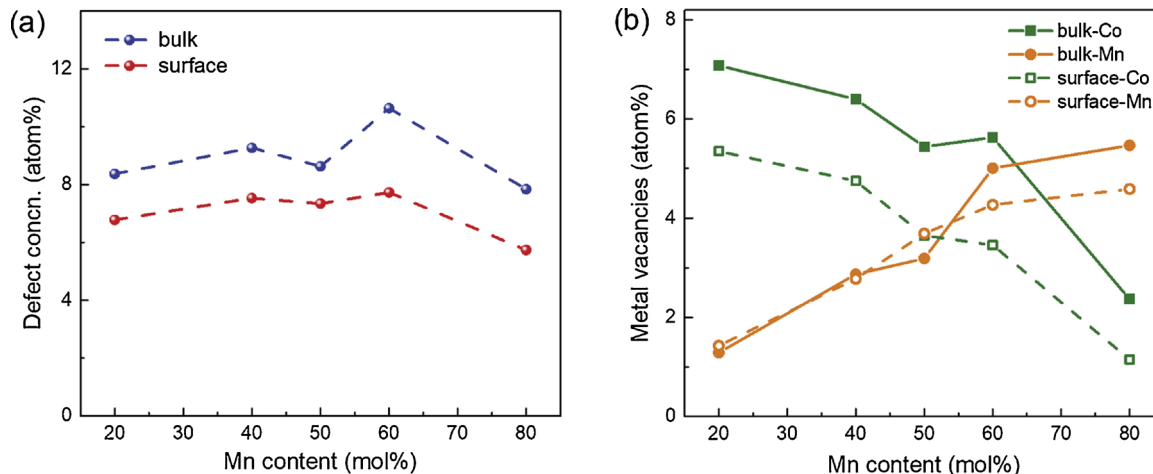


Fig. 2. Surface/bulk concentrations of (a) total metal defects, (b) Mn vacancies (orange) and Co vacancies (green) as a function of Mn content (For interpretation of the references to colour in this figure legend, the reader is referred to the web version of this article).

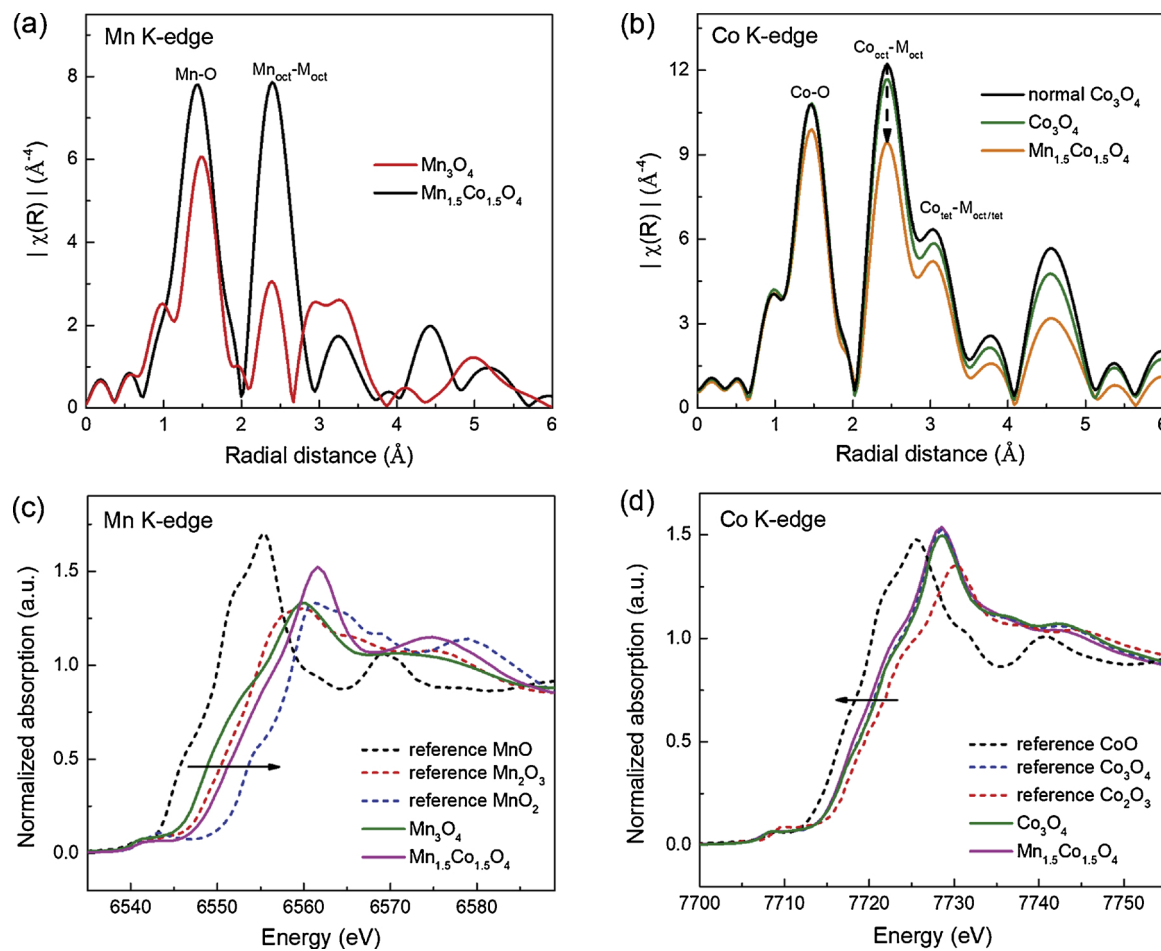


Fig. 3. Fourier transforms of (a) Mn and (b) Co K-edge EXAFS spectra for the synthesized Mn_{1.5}Co_{1.5}O₄, Mn₃O₄, Co₃O₄ and normal Co₃O₄ without defects. (M = Co or Mn; oct = octahedral sites; tet = tetrahedral sites) And (c) Mn and (d) Co K-edge XANES spectra of the synthesized Mn_{1.5}Co_{1.5}O₄, Mn₃O₄, Co₃O₄ (solid lines) and reference oxides (dotted lines).

outperforms the benchmark Pt/C (0.813 V). Moreover, Mn_{1.5}Co_{1.5}O₄ exhibits the highest limiting current density of 5.98 mA cm⁻², surpassing Pt/C (5.68 mA cm⁻²) and other Mn_xCo_{3-x}O₄. The best ORR performance of Mn_{1.5}Co_{1.5}O₄ is also revealed by the maximum loop of cyclic voltammetry (CV) curve (Fig. S5), indicating the highest current density yielded at defined overpotential.

Further evaluation of the ORR catalytic efficiency was performed by determining the electron transfer number (*n*) and yield of peroxide species from the ring and disk current recorded on rotating ring-disk electrode (RRDE) (Fig. 4c). Mn_{1.5}Co_{1.5}O₄ exhibits the highest disk current (O₂ reduction [10]) and quite small ring current (peroxide oxidation [10]). From Fig. 4d, the *n* values are calculated to be above 3.9 in the range of 0.40 to 0.85 V and the percentages of generated peroxide species are below 5% for all Mn_xCo_{3-x}O₄, indicating a desirable quasi-four electron ORR pathway, which is consistent with the results derived from the Koutecky-Levich (K-L) plots (Fig. S6). Then, the electrochemical active surface area (ECSA) was evaluated by double layer capacitance (*C_{dl}*) via CV technique (Fig. S7). Among Mn_xCo_{3-x}O₄ with different Mn/Co ratios, Mn_{1.5}Co_{1.5}O₄ shows the highest capacitance and thus the largest ECSA, indicating more active sites for catalyzing ORR.

The electrical conductivity, a key factor affecting ORR performance, was evaluated by Nyquist plots of electrical impedance spectroscopy (EIS), where the semicircular diameter reflects the electron transfer resistance. According to Fig. 4e and S8, the charge transfer resistances follow the order of Mn_{1.5}Co_{1.5}O₄ < Mn_{1.8}Co_{1.2}O₄ < Mn_{1.2}Co_{1.8}O₄ < Mn_{0.6}Co_{2.4}O₄ < Mn_{2.4}Co_{0.6}O₄ < Mn₃O₄ < < Co₃O₄, elucidating

the superior electron transfer and significantly improved conductivity of Mn_{1.5}Co_{1.5}O₄ due to enhanced electron hopping through mixed metal cations [23,43,51,52]. The durability is also an important indicator of catalytic performance, which was investigated by chronamperometric measurement in O₂-saturated 0.1 M KOH (Fig. 4f) at 1600 rpm. Importantly, Mn_{1.5}Co_{1.5}O₄ (retaining ca. 97% after 20,000 s test) exhibits much better stability than Pt/C (ca. 88%), showing promising potential to replace noble metal catalysts for practical application.

3.4. Revealing the role of metal defects in Mn_xCo_{3-x}O₄ for ORR

For the fabrication of metal defected samples, one of the key factors is the applied calcined temperature (*T*) of glycerolate precursors: first, *T* should be high enough for totally remove C and H atoms; then, a higher *T* will lead to recrystallization of the crystal lattice and decrease in defect concentrations [26,28]. In view of the above-mentioned optimal Mn/Co ratio of 1/1, the control samples with tunable defect concentrations were obtained by calcination of Mn_{1.5}Co_{1.5}Gly at 500 and 700 °C (i.e. MC-500 and MC-700) to investigate the role of metal defects in ORR. As shown in Fig. 5a, XRD patterns of MC-300, MC-500 and MC-700 show a same configuration but different diffraction peak positions due to the varied degree of lattice shrinkage caused by different defect concentrations [1]. The diffraction peaks appearing in MC-700 can be well indexed to cubic MnCo₂O₄ (JCPDS no. 23-1237), while the diffraction patterns of MC-300 and MC-500 are close to cubic MnCo₂O_{4.5} (JCPDS no. 32-0297). It should be mentioned that, the reason why the

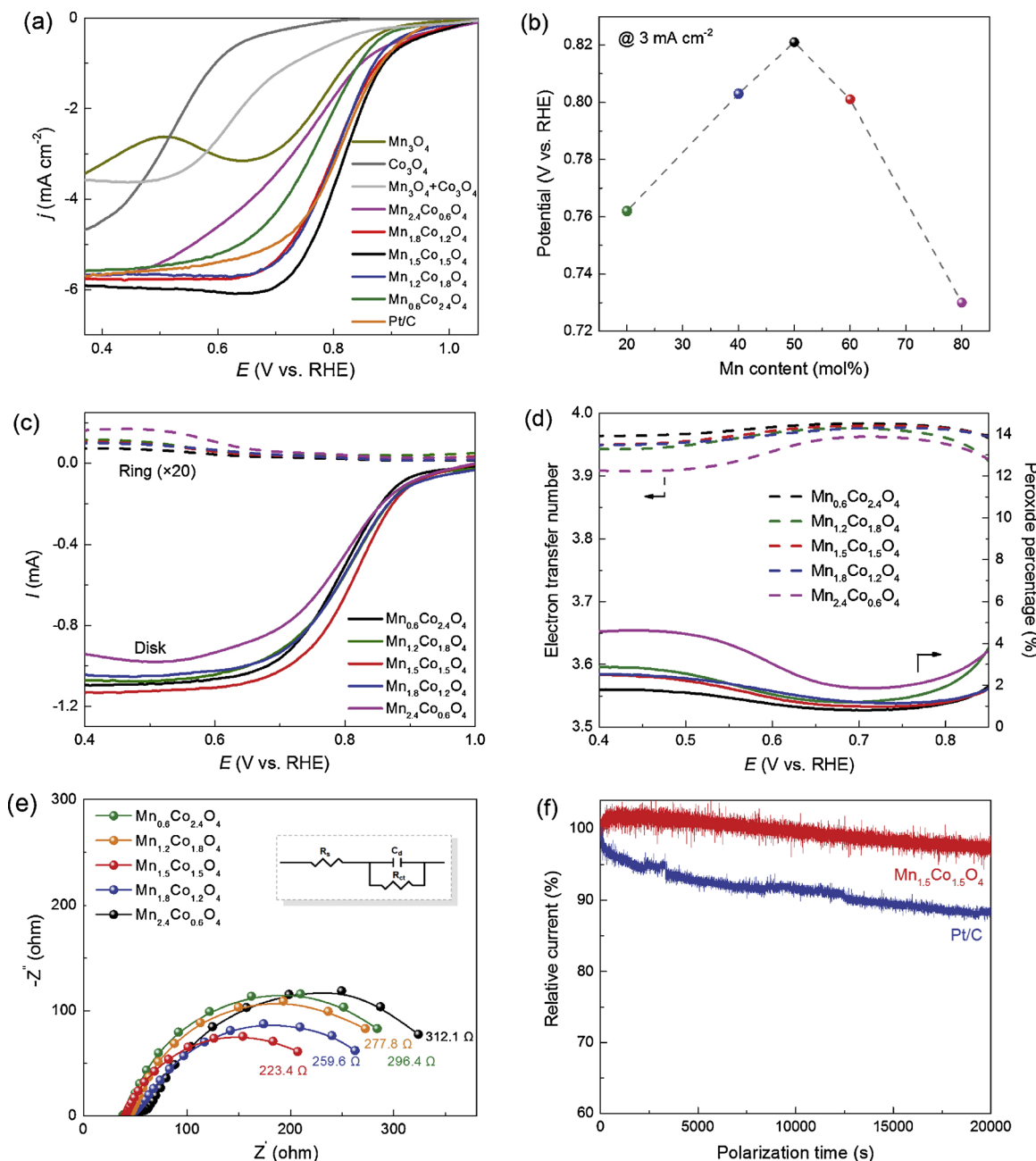


Fig. 4. ORR performance of $\text{Mn}_x\text{Co}_{3-x}\text{O}_4$ with different Mn content. (a) Rotating-disk electrode (RDE) voltammograms in O_2 -saturated 0.1 M KOH with a scan rate of 10 mV s^{-1} at 1600 rpm. (b) Potentials @ 3 mA cm^{-2} obtained from (a) as a function of Mn content. (c) Rotating ring-disk electrode (RRDE) voltammograms in O_2 -saturated 0.1 M KOH with a scan rate of 10 mV s^{-1} at 1600 rpm. The ring potential was set as 1.3 V vs. RHE. (d) Peroxide yield (solid curves) and electron transfer number (dashed lines) at various potentials. (e) Electrochemical impedance spectra (EIS) (inset: equivalent circuit model; R_{ct} , charge-transfer resistance; R_s , electrolyte resistance; C_d , capacitive reactance). (f) Chronoamperometric responses of $\text{Mn}_{1.5}\text{Co}_{1.5}\text{O}_4$ and Pt/C at 0.6 V (vs. RHE) in O_2 -saturated 0.1 M KOH at 1600 rpm.

peaks of MC-300 slightly shift to smaller angles compared with MnCo_2O_4 .5 is that the actual Mn/Co ratio is a little higher than 1/2. As reported, the oxygen-excess nonstoichiometry in spinel oxide could be ascribed to cation deficiencies rather than oxygen interstitial because the formation of cation vacancies is more thermodynamically favorable [53]. Hence, based on the degree of peak deviation from normal MnCo_2O_4 , the metal defect concentrations are in the order of MC-300 > MC-500 > MC-700, as further confirmed by the atomic ratio of metal to oxygen determined by ICP and XPS (Table 2). All three samples show almost the same Mn/Co ratio, which is 1/2 in bulk but 1/1 on the surface. The (Mn + Co)/O ratio of MC-700 is very close to the stoichiometric composition (0.75), indicating the absence of metal defects for the high- T recrystallization. However, both MC-300 and MC-500

show relatively lower (Mn + Co)/O ratios, especially in the case of MC-300 with $\sim 7.3 \text{ mol\%}$ metal defects. Furthermore, the content of V_{Mn} and V_{Co} in metal-defected MC-300 and MC-500 is quite similar, both showing 50% V_{Mn} on the surface and 35% V_{Mn} in bulk (Table S4).

As shown in Fig. 5b-d (XPS), compared with MC-700 without defects, a positive peak shift (for the lowered electron cloud density) with increasing defect concentrations is observed in O 1 s, Mn 2p and Co 2p spectra, which is consistent with previous reports [31,32,54]. DFT calculations also confirm that the neighboring O and metal atoms of metal vacancies get fewer electrons compared with those in the normal sites [31,32,42].

As exhibited in Fig. 6a, the electrocatalytic ORR performances show a positive correlation with the defect concentrations. MC-300 with the

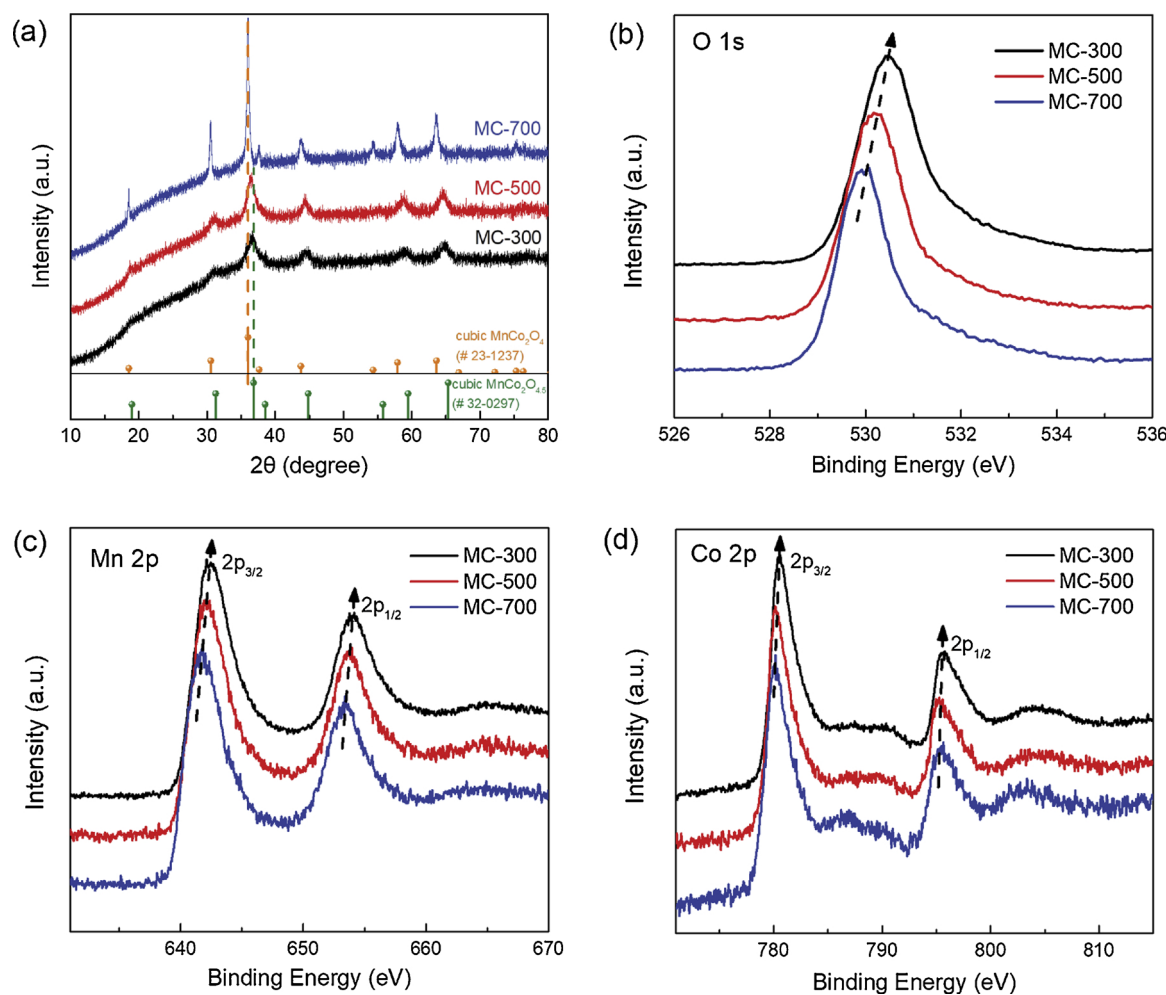


Fig. 5. (a) XRD patterns, (b) O 1s, (c) Mn 2p and (d) Co 2p XPS spectra of MC-300, MC-500 and MC-700.

Table 2
Surface and bulk elemental compositions of MC-300, MC-500 and MC-700.

Samples	Surface	Bulk	Mn/Co atomic ratio	(Mn + Co)/O atomic ratio				Defect concn. (%)		
				designed ratio	XPS	ICP	XPS	ICP	surface	bulk
MC-300	$\text{Mn}_{1.51}\text{Co}_{1.49}\text{O}_4$	$\text{Mn}_{1.11}\text{Co}_{1.89}\text{O}_4$	1.03		1.02	0.59	0.63	0.61	7.34	8.63
MC-500	$\text{Mn}_{1.55}\text{Co}_{1.45}\text{O}_4$	$\text{Mn}_{1.06}\text{Co}_{1.94}\text{O}_4$	1.03		1.07	0.55	0.68	0.67	4.46	4.97
MC-700	$\text{Mn}_{1.57}\text{Co}_{1.43}\text{O}_4$	$\text{Mn}_{1.11}\text{Co}_{1.89}\text{O}_4$	1.03		1.10	0.58	0.74	0.75	0.30	0.11

highest metal defect concentration (7.3 mol%) exhibits a remarkably improved activity in terms of lower overpotential ($E_{@3 \text{ mA cm}^{-2}}$, 0.822 V vs. RHE) and higher limiting current density (j_L , 5.98 mA cm^{-2}) than MC-700 without defects ($E_{@3 \text{ mA cm}^{-2}}$, 0.769 V; j_L , 4.60 mA cm^{-2}). The calculated Tafel slopes are in the order of MC-300 (63 mV dec^{-1}) < MC-500 (74 mV dec^{-1}) < MC-700 (90 mV dec^{-1}), indicating the presence of metal defects can significantly improve ORR kinetics. Then, the selectivity of ORR was further evaluated by RRDE measurements (Fig. S9c). Both MC-300 and MC-500 exhibit lower peroxide percentage and larger electron transfer number than MC-700 (Fig. 6b), suggesting a more favorable four-electron pathway. Moreover, the ECSAs of MC-300 and MC-500 estimated by double layer capacitance (C_{dl}) are much higher than MC-700 (Fig. S12), revealing more active catalytic sites with the presence of metal defects.

As reported in our recent work [28], metal defects can result in obvious electronic delocalization, confirmed by increased density of electronic states near Fermi level, leading to faster carrier transport

along the defective conducting channels. This phenomenon is also verified by electrochemical impedance spectroscopy (EIS) in this work. As shown in Fig. 7a, the resistance decreases with the increase of defect concentrations. Especially, the introduction of metal defects for MC-300 possesses much lower resistance than MC-700 without defects, confirming metal defects can greatly promote the electrical conductivity through charge transfer along the defective conducting channels.

Notably, the ORR process starts with adsorption and activation of O_2 , which is considered as a crucial step of ORR [2,55]. Hence, O_2 adsorption affinity is a key factor that determines ORR performance, which can be characterized by $\text{O}_2\text{-TPD}$. As shown in Fig. 7b, three desorption peaks are observed except for MC-700 (the third peak may locate above 700 °C which can be seen from the rising trend at 700 °C). The first desorption peak below 200 °C is indicative of the oxygen adsorbates while the others locate above 400 °C and 500 °C can be ascribed to the release of surface and bulk lattice oxygen, respectively [12,56]. It's obvious that MC-300 and MC-500 exhibit much higher

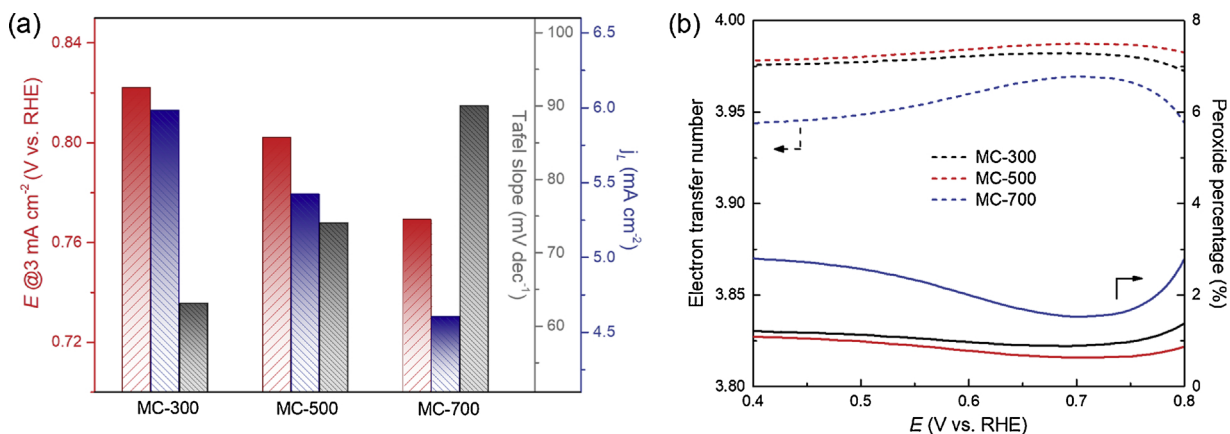


Fig. 6. ORR performance of MC-300 (with 7.34% metal defects), MC-500 (4.46%) and MC-700 (0.30%). (a) The potential @ 3 mA cm^{-2} (red), limiting current density (j_L , blue) and Tafel slopes (gray) obtained from Fig. S9. (b) Peroxide yield (solid curves) and electron transfer number (dashed lines) at various potentials (For interpretation of the references to colour in this figure legend, the reader is referred to the web version of this article).

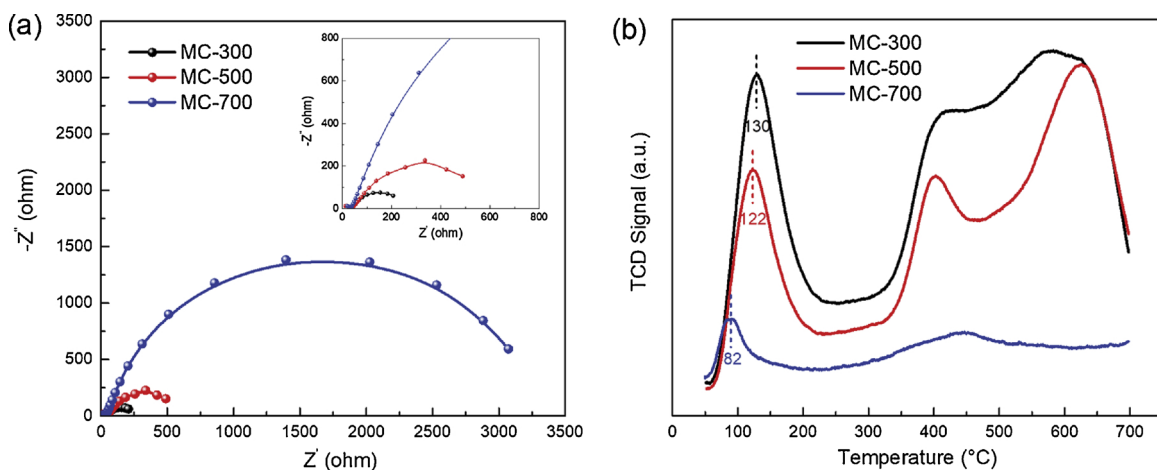


Fig. 7. (a) Electrochemical impedance spectra (EIS) (Inset is the magnified pattern of black curve) and (b) O₂-TPD profiles of MC-300, MC-500 and MC-700.

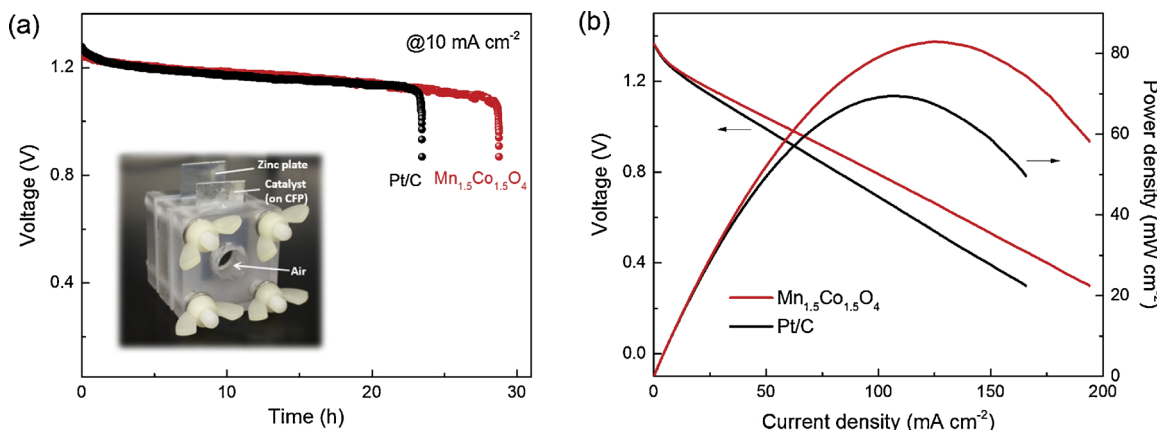


Fig. 8. (a) Galvanostatic discharge curves (inset: photograph of assembled Zn-air battery) and (b) polarization and corresponding power density curves of primary Zn-air batteries using $\text{Mn}_{1.5}\text{Co}_{1.5}\text{O}_4$ and Pt/C as the cathode catalyst.

desorption temperature (130 °C for MC-300; 122 °C for MC-500) and stronger signal intensity for the release of oxygen adsorbates, indicating a much stronger oxygen binding ability than MC-700 (~82 °C). Moreover, MC-300 with more defects shows stronger oxygen adsorption than MC-500, further confirming that metal defects can greatly enhance O₂ adsorption ability, which is beneficial for ORR.

3.5. Zn-air battery performance

As mentioned above, defected $\text{Mn}_{1.5}\text{Co}_{1.5}\text{O}_4$ shows superior ORR activity to the benchmark Pt/C and also performs well among previously reported metal oxide catalysts (Table S5). To further investigate the practical application of metal-defected $\text{Mn}_{1.5}\text{Co}_{1.5}\text{O}_4$, the primary

Zn-air batteries were constructed using a polished zinc plate as the anode, the $Mn_{1.5}Co_{1.5}O_4$ or Pt/C catalyst electrode as the air cathode, and aqueous KOH (6 M) as an electrolyte. As shown in Fig. 8a, $Mn_{1.5}Co_{1.5}O_4$ shows a similar galvanostatic discharge voltage plateaus (~ 1.2 V), but a longer discharging time (~ 29 h) as well as higher discharge capacity (~ 173 mA h) than the benchmark Pt/C (~ 23.5 h, 140 mA h), confirming its superb catalytic activity and stability for ORR. Fig. 8b presents polarization and corresponding power density curves for $Mn_{1.5}Co_{1.5}O_4$ and Pt/C catalysts. $Mn_{1.5}Co_{1.5}O_4$ shows a current density of 124.7 mA cm^{-2} with a peak power density of 82.9 mW cm^{-2} , superior to those of Pt/C (106.1 mA cm^{-2} and 69.5 mW cm^{-2}), indicating an excellent Zn-air battery performance for future application.

4. Conclusions

In this work, we successfully introduced metal defects (V_{Mn} and V_{Co}) into bimetal spinel $Mn_xCo_{3-x}O_4$ to modulate the electronic structure as highly efficient ORR and Zn-air battery electrocatalysts. The Mn-Co glycerolate precursors play a key role in constructing metal defected crystals for their O-rich lamellated crystal structures. Determined by the formation rate difference of MnGly and CoGly, a unique Mn-enriched surface is formed after thermal calcination, bringing about abundant surface active sites and optimal bulk conductivity. Moreover, V_{Mn} and V_{Co} in $Mn_xCo_{3-x}O_4$ are produced with equal formation possibility, showing a positive correlation with Mn and Co content respectively. Importantly, the presence of metal defects provides more active sites with increased electrical conductivity (caused by the improved electronic delocalization) and O_2 adsorption ability, leading to remarkably improved ORR activity and Zn-air battery performance which outperforms the benchmark Pt/C. Our work presents metal-defected oxides as a novel promising cathode material for metal-air batteries and may inspire more theoretical and experimental studies on rational defect engineering of multi-component transition metal spinels.

Acknowledgements

The authors appreciate the support from the National Natural Science Foundation of China (21506156, 21676193, 51661145026) and the Tianjin Municipal Natural Science Foundation (16JCQNJC05200, 15JCZDJC37300). We also appreciate the help of XAS analysis from Beijing Synchrotron Radiation, Institute of High Energy Physics, Chinese Academy of Sciences, Beijing, China.

Appendix A. Supplementary data

Supplementary material related to this article can be found, in the online version, at doi:<https://doi.org/10.1016/j.apcatb.2018.11.072>.

References

- Y.L. Zhu, W. Zhou, J. Yu, Y.B. Chen, M.L. Liu, Z.P. Shao, Enhancing electrocatalytic activity of perovskite oxides by tuning cation deficiency for oxygen reduction and evolution reactions, *Chem. Mater.* 28 (2016) 1691–1697.
- J. Suntivich, H.A. Gasteiger, N. Yabuuchi, H. Nakanishi, J.B. Goodenough, Y. Shao-Horn, Design principles for oxygen-reduction activity on perovskite oxide catalysts for fuel cells and metal-air batteries, *Nat. Chem.* 3 (2011) 546–550.
- Q. Wang, L. Shang, R. Shi, X. Zhang, Y. Zhao, G.I.N. Waterhouse, L.-Z. Wu, C.-H. Tung, T.-R. Zhang, NiFe layered double hydroxide nanoparticles on Co, N-codoped carbon nanoframes as efficient bifunctional catalysts for rechargeable zinc-air batteries, *Adv. Energy Mater.* 7 (2017) 1700467.
- Q. Wang, L. Shang, R. Shi, X. Zhang, G.I.N. Waterhouse, L.-Z. Wu, C.-H. Tung, T.-R. Zhang, 3D carbon nanoframe scaffold-immobilized Ni_3FeN nanoparticle electrocatalysts for rechargeable zinc-air batteries' cathodes, *Nano Energy* 40 (2017) 382–389.
- W. Xia, A. Mahmood, Z. Liang, R. Zou, S. Guo, Earth-abundant nanomaterials for oxygen reduction, *Angew. Chem. Int. Ed.* 55 (2016) 2650–2676.
- L. Shang, H. Yu, X. Huang, T. Bian, R. Shi, Y. Zhao, G.I. Waterhouse, L.Z. Wu, C.H. Tung, T.-R. Zhang, Well-dispersed Co,N-Co-doped carbon nanoframes through mesoporous-silica-protected calcination as efficient oxygen reduction electrocatalysts, *Adv. Mater.* 28 (2016) 1668–1674.
- L.M. Uhlig, G. Sievers, V. Brüser, A. Dyck, G. Wittstock, Characterization of different plasma-treated cobalt oxide catalysts for oxygen reduction reaction in alkaline media, *Sci. Bull.* 61 (2016) 612–618.
- M. Shao, Q. Chang, J.P. Dodelet, R. Chenitz, Recent advances in electrocatalysts for oxygen reduction reaction, *Chem. Rev.* 116 (2016) 3594–3657.
- T. Li, B. Xue, B. Wang, G. Guo, D. Han, Y. Yan, A. Dong, Tubular monolayer superlattices of hollow Mn_3O_4 nanocrystals and their oxygen reduction activity, *J. Am. Chem. Soc.* 139 (2017) 12133–12136.
- Y. Liang, H. Wang, J. Zhou, Y. Li, J. Wang, T. Regier, H. Dai, Covalent hybrid of spinel manganese-cobalt oxide and graphene as advanced oxygen reduction electrocatalysts, *J. Am. Chem. Soc.* 134 (2012) 3517–3523.
- Y. Liang, Y. Li, H. Wang, J. Zhou, J. Wang, T. Regier, H. Dai, Co_3O_4 nanocrystals on graphene as a synergistic catalyst for oxygen reduction reaction, *Nat. Mater.* 10 (2011) 780–786.
- F. Cheng, J. Shen, B. Peng, Y. Pan, Z. Tao, J. Chen, Rapid room-temperature synthesis of nanocrystalline spinels as oxygen reduction and evolution electrocatalysts, *Nat. Chem.* 3 (2011) 79–84.
- C. Li, X. Han, F. Cheng, Y. Hu, C. Chen, J. Chen, Phase and composition controllable synthesis of cobalt manganese spinel nanoparticles towards efficient oxygen electrocatalysis, *Nat. Commun.* 6 (2015) 7345.
- H. Wang, R. Liu, Y. Li, X. Lü, Q. Wang, S. Zhao, K. Yuan, Z. Cui, X. Li, S. Xin, R. Zhang, M. Lei, Z. Lin, Durable and efficient hollow porous oxide spinel microspheres for oxygen reduction, *Joule* 2 (2018) 337–348.
- S. Peng, X. Han, L. Li, S. Chou, D. Ji, H. Huang, Y. Du, J. Liu, S. Ramakrishna, Electronic and defective engineering of electrosprayed $CaMnO_3$ nanotubes for enhanced oxygen electrocatalysis in rechargeable zinc-air batteries, *Adv. Energy Mater.* (2018) 1800612.
- Y.-Z. Jin, Z. Li, J.-Q. Wang, R. Li, Z.-Q. Li, H. Liu, J. Mao, C.-K. Dong, J. Yang, S.-Z. Qiao, X.-W. Du, Tuning spin state of rock-salt-based oxides by manipulation of crystallinity for efficient oxygen electrocatalysis, *Adv. Energy Mater.* (2018) 1703469.
- J. Pandey, B. Hua, W. Ng, Y. Yang, K. van der Veen, J. Chen, N.J. Geels, J.L. Luo, G. Rothenberg, N. Yan, Developing hierarchically porous MnO_x/NC hybrid nanorods for oxygen reduction and evolution catalysis, *Green Chem.* 19 (2017) 2793–2797.
- Y. Liang, H. Wang, P. Diao, W. Chang, G. Hong, Y. Li, M. Gong, L. Xie, J. Zhou, J. Wang, T.Z. Regier, F. Wei, H. Dai, Oxygen reduction electrocatalyst based on strongly coupled cobalt oxide nanocrystals and carbon nanotubes, *J. Am. Chem. Soc.* 134 (2012) 15849–15857.
- Q. Zhao, Z. Yan, C. Chen, J. Chen, Spins: controlled preparation, oxygen reduction/evolution reaction application, and beyond, *Chem. Rev.* 117 (2017) 10121–10211.
- J. Duan, S. Chen, S. Dai, S.Z. Qiao, Shape control of Mn_3O_4 nanoparticles on nitrogen-doped graphene for enhanced oxygen reduction activity, *Adv. Funct. Mater.* 24 (2014) 2072–2078.
- J. Duan, Y. Zheng, S. Chen, Y. Tang, M. Jaroniec, S. Qiao, Mesoporous hybrid material composed of Mn_3O_4 nanoparticles on nitrogen-doped graphene for highly efficient oxygen reduction reaction, *Chem. Commun.* 49 (2013) 7705–7707.
- P.W. Menezes, A. Indra, D. Gonzalez-Flores, N.R. Sahraie, I. Zaharieva, M. Schwarze, P. Strasser, H. Dau, M. Driess, High-performance oxygen redox catalyst with multifunctional cobalt oxide nanochains: morphology-dependent activity, *ACS Catal.* 5 (2015) 2017–2027.
- E. Lee, J.H. Jang, Y.U. Kwon, Composition effects of spinel $Mn_xCo_{3-x}O_4$ nanoparticles on their electrocatalytic properties in oxygen reduction reaction in alkaline media, *J. Power Sources* 273 (2015) 735–741.
- C. Yuan, H.B. Wu, Y. Xie, X.W. Lou, Mixed transition-metal oxides: design, synthesis, and energy-related applications, *Angew. Chem. Int. Ed.* 53 (2014) 1488–1504.
- Y.W. Liu, C. Xiao, P.C. Huang, M. Cheng, Y. Xie, Regulating the charge and spin ordering of two-dimensional ultrathin solids for electrocatalytic water splitting, *Chemistry* 4 (2018) 1263–1283.
- H. Wang, J. Zhang, X. Hang, X. Zhang, J. Xie, B. Pan, Y. Xie, Half-metallicity in single-layered manganese dioxide nanosheets by defect engineering, *Angew. Chem. Int. Ed.* 54 (2015) 1195–1199.
- L. Pan, S.B. Wang, J.W. Xie, L. Wang, X.W. Zhang, J.-J. Zou, Constructing TiO_2 p-n homojunction for photoelectrochemical and photocatalytic hydrogen generation, *Nano Energy* 28 (2016) 296–303.
- R.R. Zhang, Y.C. Zhang, L. Pan, G.Q. Shen, N. Mahmood, Y.H. Ma, Y. Shi, W.Y. Jia, L. Wang, X.W. Zhang, W. Xu, J.-J. Zou, Engineering cobalt defects in cobalt oxide for highly efficient electrocatalytic oxygen evolution, *ACS Catal.* 8 (2018) 3803–3811.
- D. Yan, Y. Li, J. Huo, R. Chen, L. Dai, S. Wang, Defect chemistry of nonprecious-metal electrocatalysts for oxygen reactions, *Adv. Mater.* 29 (2017) 1606459.
- Y. Zhao, X. Jia, G. Chen, L. Shang, G.I. Waterhouse, L.Z. Wu, C.H. Tung, D. O'Hare, T. Zhang, Ultrafine NiO nanosheets stabilized by TiO_2 from monolayer NiTi-LDH precursors: an active water oxidation electrocatalyst, *J. Am. Chem. Soc.* 138 (2016) 6517–6524.
- L. Pan, S.B. Wang, W.B. Mi, J.J. Song, J.-J. Zou, L. Wang, X.W. Zhang, Undoped ZnO abundant with metal vacancies, *Nano Energy* 9 (2014) 71–79.
- S. Wang, L. Pan, J.J. Song, W. Mi, J.-J. Zou, L. Wang, X. Zhang, Titanium-defected undoped anatase TiO_2 with p-type conductivity, room-temperature ferromagnetism, and remarkable photocatalytic performance, *J. Am. Chem. Soc.* 137 (2015) 2975–2983.
- P.C. Lau, T.L. Kwong, K.F. Yung, Effective heterogeneous transition metal glycerolates catalysts for one-step biodiesel production from low grade non-refined Jatropha oil and crude aqueous bioethanol, *Sci. Rep.* 6 (2016) 23822.

[34] O. Jankovský, D. Sedmidubský, P. Šimek, Z. Sofer, P. Ulbrich, V. Bartuňek, Synthesis of MnO , Mn_2O_3 and Mn_3O_4 nanocrystal clusters by thermal decomposition of manganese glycerolate, *Ceram. Int.* 41 (2015) 595–601.

[35] T. Brylewski, W. Kuczka, A. Adamczyk, A. Kruk, M. Stygar, M. Bobruk, J. Dąbrowa, Microstructure and electrical properties of $\text{Mn}_{1+x}\text{Co}_{2-x}\text{O}_4$ ($0 \leq x \leq 1.5$) spinels synthesized using EDTA-gel processes, *Ceram. Int.* 40 (2014) 13873–13882.

[36] C. Wei, Z. Feng, G.G. Scherer, J. Barber, Y. Shao-Horn, Z.J. Xu, Cations in octahedral sites: a descriptor for oxygen electrocatalysis on transition-metal spinels, *Adv. Mater.* 29 (2017) 1606800.

[37] P.G. Slade, E.W. Radoslovich, M. Raupach, Crystal and molecular structure of cobalt (II) monoglycerolate, *Acta Crystallogr. B* 27 (1971) 2432–2436.

[38] E.W. Radoslovich, M. Raupach, P.G. Slade, R.M. Taylor, Crystalline cobalt, zinc, manganese, and iron alkoxides of glycerol, *Aust. J. Chem.* 23 (1970) 1963–1971.

[39] R.P. Eckberg, W.E. Hatfield, D.B. Losee, Unusual magnetic properties of polymeric cobalt (II) monoglycerolate, a compound containing alkoxo-bridged cobalt (II) ions, *Inorg. Chem.* 13 (1974) 740–742.

[40] T.W. Turney, A. Patti, W. Gates, U. Shaheen, S. Kulasegaram, Formation of glycerol carbonate from glycerol and urea catalyzed by metal monoglycerolates, *Green Chem.* 15 (2013) 1925–1931.

[41] B.J. Morgan, G.W. Watson, Polaronic trapping of electrons and holes by native defects in anatase TiO_2 , *Phys. Rev. B* 80 (2009) 233102.

[42] S. Na-Phattalung, M.F. Smith, K. Kim, M.-H. Du, S.-H. Wei, S.B. Zhang, S. Limpijumpong, First-principles study of native defects in anatase TiO_2 , *Phys. Rev. B* 73 (2006) 125205.

[43] Y. Zhou, S. Sun, S. Xi, Y. Duan, T. Sritharan, Y. Du, Z.J. Xu, Superexchange effects on oxygen reduction activity of edge-sharing $[\text{Co}_x\text{Mn}_{1-x}\text{O}_6]$ octahedra in spinel oxide, *Adv. Mater.* 30 (2018) 1705407.

[44] D. Carta, M.F. Casula, A. Falqui, D. Loche, G. Mountjoy, C. Sangregorio, A. Corrias, A structural and magnetic investigation of the inversion degree in ferrite nanocrystals MFe_2O_4 ($\text{M} = \text{Mn, Co, Ni}$), *J. Phys. Chem. C* 113 (2009) 8606–8615.

[45] S. Calvin, E.E. Carpenter, B. Ravel, V.G. Harris, S.A. Morrison, Multiedge refinement of extended x-ray-absorption fine structure of manganese zinc ferrite nanoparticles, *Phys. Rev. B* 66 (2002) 224405.

[46] Q.W. Tang, L.H. Jiang, J. Liu, S.L. Wang, G.Q. Sun, Effect of surface manganese valence of manganese oxides on the activity of the oxygen reduction reaction in alkaline media, *ACS Catal.* 4 (2014) 457–463.

[47] K. Lei, X. Han, Y. Hu, X. Liu, L. Cong, F. Cheng, J. Chen, Chemical etching of manganese oxides for electrocatalytic oxygen reduction reaction, *Chem. Commun.* 51 (2015) 11599–11602.

[48] L.Q. Mao, D. Zhang, T. Sotomura, K. Nakatsu, N. Koshiba, T. Ohsaka, Mechanistic study of the reduction of oxygen in air electrode with manganese oxides as electrocatalysts, *Electrochim. Acta* 48 (2003) 1015–1021.

[49] H.Y. Su, Y. Gorlin, I.C. Man, F. Calle-Vallejo, J.K. Norskov, T.F. Jaramillo, J. Rossmeisl, Identifying active surface phases for metal oxide electrocatalysts: a study of manganese oxide bi-functional catalysts for oxygen reduction and water oxidation catalysis, *Phys. Chem. Chem. Phys.* 14 (2012) 14010–14022.

[50] J. Xiao, Q. Kuang, S. Yang, F. Xiao, S. Wang, L. Guo, Surface structure dependent electrocatalytic activity of Co_3O_4 anchored on graphene sheets toward oxygen reduction reaction, *Sci. Rep.* 3 (2013) 2300.

[51] E. Rios, J.-L. Gautier, G. Poillerat, P. Chartier, Mixed valency spinel oxides of transition metals and electrocatalysis: case of the $\text{Mn}_x\text{Co}_{3-x}\text{O}_4$ system, *Electrochim. Acta* 44 (1998) 1491–1497.

[52] C.C. Kuo, W.J. Lan, C.H. Chen, Redox preparation of mixed-valence cobalt manganese oxide nanostructured materials: highly efficient noble metal-free electrocatalysts for sensing hydrogen peroxide, *Nanoscale* 6 (2014) 334–341.

[53] Y. Zhou, S. Sun, J. Song, S. Xi, B. Chen, Y. Du, A.C. Fisher, F. Cheng, X. Wang, H. Zhang, Z.J. Xu, Enlarged CoO covalency in octahedral sites leading to highly efficient spinel oxides for oxygen evolution reaction, *Adv. Mater.* 30 (2018) 1802912.

[54] J. Wang, J. Li, C. Jiang, P. Zhou, P. Zhang, J. Yu, The effect of manganese vacancy in birnessite-type MnO_2 on room-temperature oxidation of formaldehyde in air, *Appl. Catal. B Environ.* 204 (2017) 147–155.

[55] J. Suntivich, K.J. May, H.A. Gasteiger, J.B. Goodenough, Y. Shao-Horn, A perovskite oxide optimized for oxygen evolution catalysis from molecular orbital principles, *Science* 334 (2011) 1383–1385.

[56] Y. Wang, H. Arandiyani, Y. Liu, Y. Liang, Y. Peng, S. Bartlett, H. Dai, S. Rostamnia, J. Li, Template-free scalable synthesis of flower-like $\text{Co}_{3-x}\text{Mn}_x\text{O}_4$ spinel catalysts for toluene oxidation, *ChemCatChem* 10 (2018) 3429–3434.